Essay on magnetic-wind mills part I analysis and design

Essay on Magnetic-Wind Mills Part I : Analysis and Design

J. L. Duarte
Department of Electrical Engineering
Eindhoven University of Technology
The Netherlands

***Abstract*—A methodology for the synthesis of a prime mover is presented, based only on attraction/repulsion of permanent magnets. The design example is given for a demonstration prototype that has the potential to unfold the sustainable generation of $22W$ mechanical power at $1000\,rpm$ and beyond.**

I. Introduction

It is asserted in [1], on account of purely analytical equations from classical Electromagnetism, that a constrained displacement of an arrangement of filamentary current loops adds excess mechanical energy to the system moving parts, as long as the currents in the loops are kept **constant** during the closed translational orbit.

Further, as [2] vindicates, it is also possible to obtain the same theoretical results, which have been reached on the basis of the Lorentz Force law, by another calculation approach, namely the numerical solution of Maxwell stress tensors through the Finite Element Method. The outcomes with FEM confirm that an energy excess appears under constrained translational trajectories of permanent magnets (PMs). In fact, the same is valid for the Biot-Savart law and Mutual Inductance concepts, because all these methods lead to identical values when calculating forces among current loops [3], a commonly considered tool for modeling PMs.

In order to pave the way for experimental verification of the theoretical expectations above, this article presents the analysis and design of a first-principles-first prototype, idyllically denominated *a magnetic-wind mill*, being devised as the aggregation of simple prime-mover cells based on PMs. The magnets are modeled as the superposition of filamentary loops with constant current.

Accordingly, the intention in the following sections is to project a device wherein the elementary cells operating together create a persistent smooth torque, significant to deploy enough sustainable mechanical energy for conclusive measurements. So, the methodology developed hereinafter details the necessary analysis tools for this purpose. The design of a small mill is presented, aiming at generating about $22W$ when rotating at $1000\,rpm$. Future experiments are planned to confirm or invalidate the feasibility of these provocative theoretical statements.

II. Elementary prime-mover cell

The concept for an initial source of motive power is shown in Fig. 1. The gearing (this case cog-wheels), assembled to-

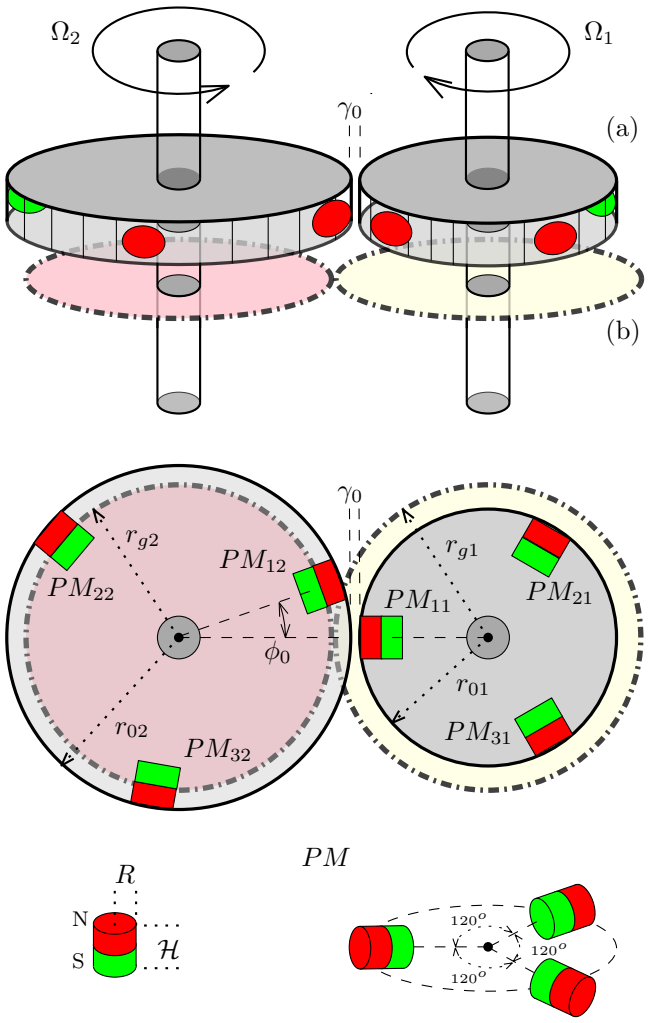

Fig. 1: Elementary prime-mover cell, consisting of (a) two rotors with embedded permanent magnets (PMs) and fixed gap separation (γ_0), and (b) a common gear mechanism, namely 1:1 cog-wheels. The angular misalignment between the rotors (ϕ_0) is kept constant by the gears in spite of rotation.

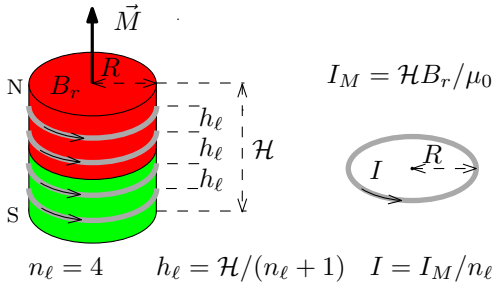

Fig. 2: Method to approximate the magnetic field created by a cylindrical PM with remanent flux density B_r as the superposition of the magnetic field engendered by n_ℓ filamentary current loops with separation h_ℓ between loops.

gether with the rotors in spinning shafts, impose a constrained translation for the permanent magnets. The resulting attraction/repulsion forces among the magnets during the translational displacement lead to asymmetric torque characteristics, as shown in the sequence. A consequence of this is that, in theory, a modular structure with stacked prime-mover cells sharing the same shafts yields the sustainable generation of mechanical energy.

III. Asymmetric Torque Characteristics

A. Modeling of a permanent magnet

The magnetic dipole is the fundamental element of magnetism. It can be thought as a small current loop with dipole moment $\vec{m}\,[Am^2]$. Statistically, one can speak about a net magnetization $\vec{M}\,[A/m]$, representing the limit ratio of dipole moments per volume of magnetic material.

Contrary to the behavior of ferromagnetic materials, in a PM with homogeneous and uniform magnetization, there is barely interaction of the magnetic dipoles with an externally applied magnetic field. The magnetization is practically constant up to a high level of external coercive field, found to be [4]

$$\vec{M} = \frac{\vec{B}_r}{\mu_0}, \tag{1}$$

where $\vec{B}_r[T]$ is the so-called remanent magnetic flux density of the material, and $\mu_0 = 4\pi \times 10^{-7}[H/m]$ the permeability of free space.

With regard to a PM specimen with cylindrical shape, like in Fig. 2, an analytical modeling technique is possible by assuming a fictitious magnetic surface current density on the magnet surface, given by

$$\vec{J}_M = \vec{M} \times \vec{n}\,[A/m], \tag{2}$$

where $\vec{n}$ is a unity vector normal to the cylindrical surface.

So, for a magnet with height $\mathcal{H}$, the total equivalent magnetizing current on the surface is found to become

$$I_M = \int_{\mathcal{H}} J_M \,\mathrm{d}h = \mathcal{H}B_r/\mu_0\;[A]. \tag{3}$$

For expedient evaluation of magnetic forces through an analytical approach, the surface current in (3) is split and lumped in n_ℓ circular current loops with separation h_ℓ between loops, as shown in Fig. 2. The resulting force between magnets is then calculated as the superposition of the forces among all the equivalent current loops.

B. Current loops with constrained displacement

Two filamentary circular current loops with inner radii R_1 and R_2 and constant currents I_1 and I_2, respectively, are shown in Fig. 3, centered at points C_1 and C_2. The loop centers may translate with constant radius, r_1 and r_2, around the pivot points P_1 and P_2, such that C_1, C_2, P_1 and P_2 remain in the same plane. By given a compulsory relationship for the radial angles ϕ_1 and ϕ_2, a constrained joint trajectory for the loops is obtained. For the purpose of analysis, convenient orthogonal vector reference frames are designated in Fig. 3.

C. Reference frames

Fig. 4 illustrates the unity vectors in Fig. 3 in a frontal perspective with regard to the translation plane, showing clearly that the unity vectors $\vec{a}_{n1}$ and $\vec{a}_{n2}$ are normal to the corresponding current loop planes.

For ease of analysis, orthogonal reference frames in Figs. 3 and 4 are defined as

$$\begin{aligned}
&\vec{a}_{xj} = \vec{a}_{yj} \times \vec{a}_{zj},\ \vec{a}_{yj} = \vec{a}_{zj} \times \vec{a}_{xj}, \vec{a}_{zj} = \vec{a}_{xj} \times \vec{a}_{yj},\\
&\vec{a}_{tj} = \vec{a}_{\ell j} \times \vec{a}_{nj},\ \vec{a}_{\ell j} = \vec{a}_{nj} \times \vec{a}_{tj}, \vec{a}_{nj} = \vec{a}_{tj} \times \vec{a}_{\ell j},\\
&\text{with}\ \ j = \{1, 2\}\ \ \text{and}\\
&\vec{a}_{x2} = -\vec{a}_{x1},\ \vec{a}_{y2} = -\vec{a}_{y1},\ \vec{a}_{z2} = \vec{a}_{z1},\\
&\vec{a}_{\ell 2} = -\vec{a}_{\ell 1},\ \vec{a}_{\ell 1} = \vec{a}_{y2}\,,
\end{aligned} \tag{4}$$

where '$\times$' denotes vector cross product.

On account of the sign convention for the radial angles ϕ_1 and ϕ_2 in Fig. 4, the transformations between reference frames follow from

$$\begin{aligned}
\begin{bmatrix}\vec{a}_{tj}\\ \vec{a}_{nj}\end{bmatrix} &= \begin{bmatrix}-\sin\phi_j & \cos\phi_j\\ \cos\phi_j & \sin\phi_j\end{bmatrix}\begin{bmatrix}\vec{a}_{xj}\\ \vec{a}_{zj}\end{bmatrix},\ j = \{1, 2\};\\
\begin{bmatrix}\vec{a}_{xj}\\ \vec{a}_{zj}\end{bmatrix} &= \begin{bmatrix}-\sin\phi_j & \cos\phi_j\\ \cos\phi_j & \sin\phi_j\end{bmatrix}\begin{bmatrix}\vec{a}_{tj}\\ \vec{a}_{nj}\end{bmatrix},\ j = \{1, 2\};\\
\begin{bmatrix}\vec{a}_{ti}\\ \vec{a}_{ni}\end{bmatrix} &= \begin{bmatrix}\sin\phi_i & \cos\phi_i\\ -\cos\phi_i & \sin\phi_i\end{bmatrix}\begin{bmatrix}\vec{a}_{xj}\\ \vec{a}_{zj}\end{bmatrix}, i, j = \{1, 2\,;\, 2, 1\};\\
\begin{bmatrix}\vec{a}_{xi}\\ \vec{a}_{zi}\end{bmatrix} &= \begin{bmatrix}\sin\phi_j & -\cos\phi_j\\ \cos\phi_j & \sin\phi_j\end{bmatrix}\begin{bmatrix}\vec{a}_{tj}\\ \vec{a}_{zj}\end{bmatrix},\ i, j = \{1, 2\,;\, 2, 1\};\\
\begin{bmatrix}\vec{a}_{ti}\\ \vec{a}_{ni}\end{bmatrix} &= \begin{bmatrix}\cos\phi_{ij} & \sin\phi_{ij}\\ \sin\phi_{ij} & -\cos\phi_{ij}\end{bmatrix}\begin{bmatrix}\vec{a}_{tj}\\ \vec{a}_{nj}\end{bmatrix},\ i, j = \{1, 2\,;\, 2, 1\};
\end{aligned} \tag{5}$$

with

$$\phi_{12} = \phi_{21} = \phi_1 + \phi_2\,. \tag{6}$$

It is also assumed in Fig. 4 that the sum $r_1 + \gamma + r_2$ is constant, being equal to

$$r_1 + \gamma + r_2 = \Sigma_0 = r_{02} + \gamma_0 + r_{01}, \tag{7}$$

where $r_1 \le r_{01},\ r_2 \le r_{02},\ \gamma \ge \gamma_0$, with r_{01}, r_{02}, γ_0 defined in Fig. 1.

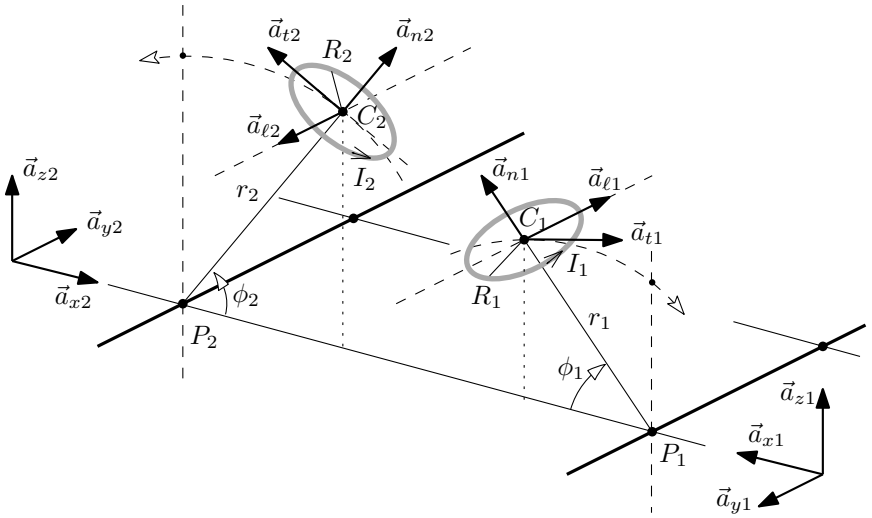

Fig. 3: Filamentary current loops with angular misalignment. The loops translate on the same plane with constant radii around fixed pivot points.

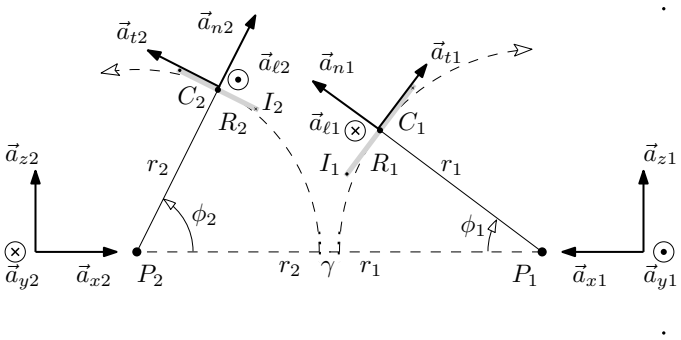

Fig. 4: Orthogonal vector reference frames from Fig. 3 shown in a frontal perspective.

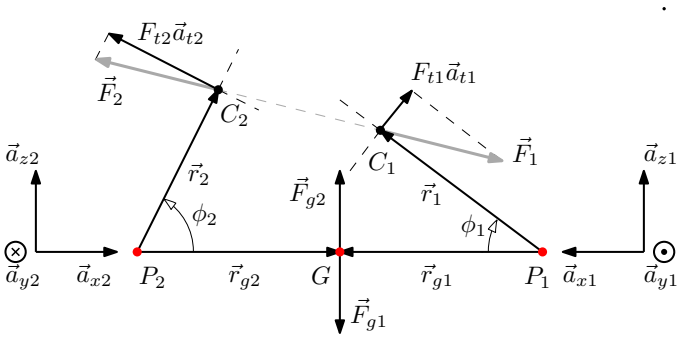

Fig. 5: Force pairs as created by magnetic repulsion/attraction between current loops constrained by cog-wheels.

As an example of frame transformation, the vector linking the loop centers C_1 to C_2, when referenced to $(\vec{a}_{t1}, \vec{a}_{n1})$, can be found from

$$\begin{aligned}
\vec{r}_{C21} &= r_2\vec{a}_{r2} + \Sigma_0\vec{a}_{x1} - r_1\vec{a}_{x1}\,, \\
\vec{r}_{C21} &= \begin{bmatrix} r_2\cos\phi_2 & r_2\sin\phi_2 \end{bmatrix}\begin{bmatrix}\vec{a}_{x2}\\ \vec{a}_{z2}\end{bmatrix} + \begin{bmatrix}\Sigma_0 & 0\end{bmatrix}\begin{bmatrix}\vec{a}_{x1}\\ \vec{a}_{z1}\end{bmatrix} + \\
&+ \begin{bmatrix} r_1\cos\phi_1 & r_1\sin\phi_1 \end{bmatrix}\begin{bmatrix}\vec{a}_{x1}\\ \vec{a}_{z1}\end{bmatrix},
\end{aligned}$$

and, taking (5), after some manipulations it is found

$$\begin{aligned}
\vec{r}_{C21} &= -\left(\Sigma_0\sin\phi_1 - r_2\sin\phi_{12}\right)\vec{a}_{t1} \\
&\quad + \left(\Sigma_0\cos\phi_1 - r_2\cos\phi_{12} - r_1\right)\vec{a}_{n1}. \qquad (8)
\end{aligned}$$

D. Static forces and torques

Fig. 5 illustrates a static situation, showing the magnetic forces on the current loops in Fig. 3 when a gearing such as cog-wheels is applied. The loop centers are located at

$$\vec{r}_1 = r_1\,\vec{a}_{n1} \;\text{ and }\; \vec{r}_2 = r_2\,\vec{a}_{n2}$$

relatively to the pivot points P_1 and P_2, respectively. Point G is fixed in space and lies on the interface contact between sides of the cog-wheels in Fig. 1, the gearing having also pivot points at P_1 and P_2 and constant radii as

$$\vec{r}_{g1} = r_{g1}\,\vec{a}_{x1} \;\text{ and }\; \vec{r}_{g2} = r_{g2}\,\vec{a}_{x2}\,.$$

Note, with regard to Fig.4 and (7), that $r_{g1} + r_{g2} = \Sigma_0$ (as an aside, also note in Fig. 1 that $r_{g1} = r_{g2}$).

The magnetic forces actuating on the current loops, $\vec{F}_1$ and $\vec{F}_2$, form an repulsion/attraction pair, that is,

$$\vec{F}_1 + \vec{F}_2 = 0. \qquad (9)$$

The reflected force $\vec{F}_{g2}$ on the gearing interface at side #2 is due to the torque created by $\vec{F}_1$ on the shaft at side #1. Otherwise stated, $\vec{F}_{g1}$ and $\vec{F}_{g2}$ are action/reaction forces on the interface of the cog-wheels, given by

$$\begin{aligned}
\vec{r}_1 \times \vec{F}_1 + \vec{r}_{g1} \times \vec{F}_{g1} &= 0, \qquad (10)\\
\vec{F}_{g1} + \vec{F}_{g2} &= 0. \qquad (11)
\end{aligned}$$

Following the approach in [3] (also detailed in [1]), it is convenient to calculate the magnetic force $\vec{F}_2$ on loop #2, that

is a consequence of current circulation through loop #1, with reference to a vectorial frame placed on loop #1 as

$$\vec{F}_2 = \mathcal{F}_{t21}\,\vec{a}_{t1} + \mathcal{F}_{n21}\,\vec{a}_{n1}, \tag{12}$$

since $\mathcal{F}_{t21} \equiv \mathcal{F}_{t21}(\phi_1,\phi_2), \mathcal{F}_{n21} \equiv \mathcal{F}_{n21}(\phi_1,\phi_2)$ may be then determined by purely analytical equations. Eventually, when necessary to consider $\vec{F}_2$ with reference to a frame placed on loop #2 as

$$\vec{F}_2 = F_{t2}\,\vec{a}_{t2} + F_{n2}\,\vec{a}_{n2}, \tag{13}$$

it results from (4) and (12) that

$$\begin{aligned}
\vec{F}_2 &= \begin{bmatrix}\mathcal{F}_{t21} & \mathcal{F}_{n21}\end{bmatrix}\begin{bmatrix}\vec{a}_{t1}\\ \vec{a}_{n1}\end{bmatrix},\\
\vec{F}_2 &= \begin{bmatrix}\mathcal{F}_{t21} & \mathcal{F}_{n21}\end{bmatrix}\begin{bmatrix}\cos\phi_{12} & \sin\phi_{12}\\ \sin\phi_{12} & -\cos\phi_{12}\end{bmatrix}\begin{bmatrix}\vec{a}_{t2}\\ \vec{a}_{n2}\end{bmatrix},
\end{aligned}$$

leading to

$$\begin{aligned}
F_{t2} &= \mathcal{F}_{t21}\cos\phi_{12} + \mathcal{F}_{n21}\sin\phi_{12}, &(14)\\
F_{n2} &= \mathcal{F}_{t21}\sin\phi_{12} - \mathcal{F}_{n21}\cos\phi_{12}\,. &(15)
\end{aligned}$$

Similarly, the force $\vec{F}_1$ exerted on loop #1 due to current circulation through loop #2 is referenced to a frame placed on loop #1 as

$$\vec{F}_1 = F_{t1}\,\vec{a}_{t1} + F_{n1}\,\vec{a}_{n1}\,. \tag{16}$$

Thereby, from (9), (12) and (16) follows

$$F_{t1} = -\mathcal{F}_{t21} \;\;\&\;\; F_{n1} = -\mathcal{F}_{n21}\,. \tag{17}$$

Once $\mathcal{F}_{t21}(\phi_1,\phi_2), \mathcal{F}_{n21}(\phi_1,\phi_2)$ are known, the associated torques in Fig. 5 can be readily described. For instance, the resulting torque $\vec{T}_2$ around the pivot point P_2 is given by

$$\begin{aligned}
\vec{T}_2 &= \vec{r}_2 \times \vec{F}_2 + \vec{r}_{g2} \times \vec{F}_{g2}, \;\; \text{or} &(18)\\
\vec{T}_2 &= -T_2(\phi_1,\phi_2)\,\vec{a}_{y2}, &(19)
\end{aligned}$$

where the minus sign in (19) has been introduced for later display convenience, indicating that $\vec{T}_2$ acts in the c.c.w. direction when $T_2(\phi_1,\phi_2) > 0$. Combining (9), (10) and (11) with (19), it is found that, after some manipulations,

$$T_2(\phi_1,\phi_2) = (r_2\cos\phi_{12} - \rho_{21}r_1)\mathcal{F}_{t21} + (r_2\sin\phi_{12})\mathcal{F}_{n21} \tag{20}$$

where $\rho_{21} = r_{g2}/r_{g1} = 1$ is the gear ratio.

When ϕ_1 and ϕ_2 are constrained as

$$\phi_1 = \rho_{21}\theta \;\;\&\;\; \phi_2 = \theta + \phi_0 \;\text{ with }\theta = \int \mathrm{d}\theta\,, \tag{21}$$

it is shown in the following section that, for a special choice of parameters,

$$\langle T_2\rangle = \frac{1}{2\pi}\int_0^{2\pi} T_2(\phi_1,\phi_2)\,\mathrm{d}\theta \neq 0\,. \tag{22}$$

Otherwise stated, the average torque $\langle T_2\rangle$ can be rendered asymmetric [2].

TABLE I: Mill parameters and geometrical dimensions

Parameter		Value	Description	Fig.
r_{01}	[mm]	21.0	outer radius rotor #1	
r_{02}	[mm]	30.0	outer radius rotor #2	
r_{g1}	[mm]	26.0	outer radius gear at side #1	(1)
r_{g2}	[mm]	26.0	outer radius gear at side #2	
γ_0	[mm]	1.0	gap between rotors	
ϕ_0	[deg]	-5^o	angle shift between rotors	
R	[mm]	5.0	radius cylindrical PM	
$\mathcal{H}$	[mm]	3.0	height cylindrical PM	
B_r	[T]	1.45	remanent flux density (NdFeB N52)	
I_M	[kA]	3.5	surface Amperian current	(2)
n_ℓ	[-]	4	number of equivalent loops	
h_ℓ	[mm]	0.60	separation between loops	
I	[kA]	0.88	current in filamentary loop	
I_1	[kA]	0.88	current in loop #1	
I_2	[kA]	0.88	current in loop #2	(3)
R_1	[mm]	5.0	radius loop #1	
R_2	[mm]	5.0	radius loop #2	
n_c	[-]	8	number of stacked cells	(9)
h_c	[mm]	12.0	vertical separation between rotors	

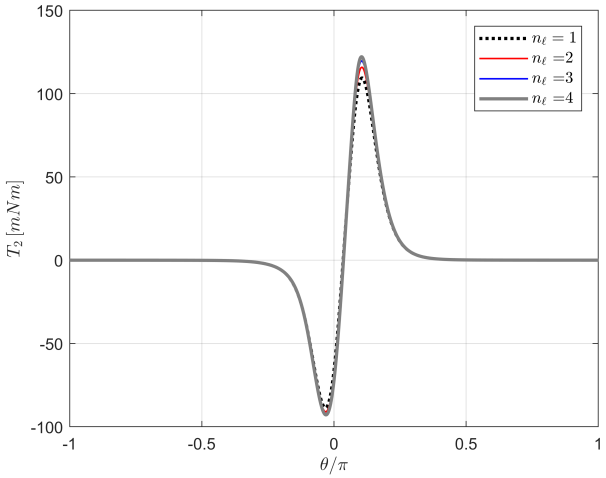

Fig. 6: Calculated static torque characteristics of a prime-mover cell with just one PM at each rotor (but keeping the radial misalignment $\phi_0 = -5^o$ between rotors, see Fig. 1). The magnets are modeled by sets of n_ℓ current loops and corresponding separation h_ℓ between loops (as in Fig. 2).

IV. Layout of the Mill

Taking into account the parameters in Table I, Fig. 6 depicts the resulting asymmetric torque profile of the prime-mover cell with only one PM per rotor (instead of 3 magnets shifted by 120^o as in Fig. 1). For the sake of comparison the PMs are modeled with different number of current loops n_ℓ, and salient numerical results are given in Table II.

TABLE II: Torque values in Fig. 6

n_ℓ	[-]	1	2	3	4	# equiv loops
h_ℓ	[mm]	1.50	1.00	0.75	0.60	loop separation
$\langle T_2\rangle$	[m Nm]	1.274	1.395	1.463	1.506	mean torque
T_2^{peak}	[m Nm]	109.4	115.8	119.6	122.1	peak torque

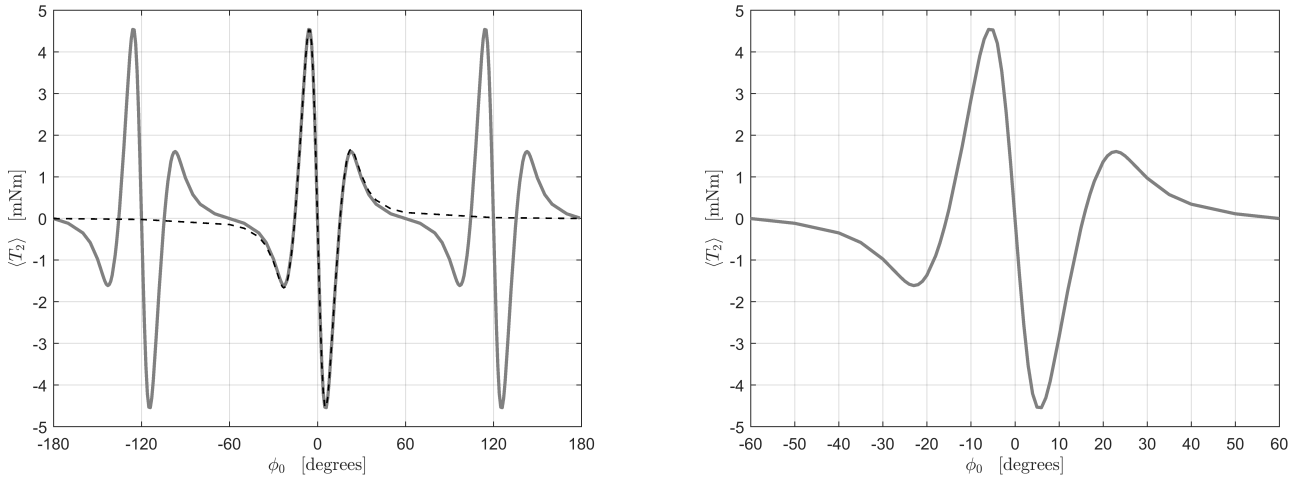

(a) (b)

Fig. 7: (a) Calculated average torque of a prime-mover cell as function of the misalignment ϕ_0 between rotors. (b) As expected from the cell symmetry (Fig. 1), the pattern in (a) repeats at intervals of 60^o. The maximum occurs for $-6^o \leq \phi_0 \leq -5^o$. The dotted trace in (a) refers to the mean torque of a simplified cell (Fig. 6 with $n_\ell = 4$).

It is possible to conclude from the outcomes in Table II that only marginal improvement in the numerical values can be expected for $n_\ell > 4$. Therefore, in the sequence it is assumed $n_\ell = 4$ in all calculations. Also note in Fig. 6 and from the results in Table II *a positive average torque systematically arises*. For instance, considering $\phi_0 = -5^o$, it follows from (22) that

$$\langle T_2 \rangle_0 = 1.506\, mNm \approx 12\%\, T_2^{peak}. \tag{23}$$

This is found to be a significant observation [1] [2].

The choice for $\phi_0 = -5^o$ in Fig. 6 has been decided in view of the local maxima in Fig. 7, where the mean torque as function of ϕ_0 is shown when a complete prime-mover cell with 3 PMs per rotor is considered. The detailed torque characteristics get the repeated pattern as depicted in Fig.8, where, again, $\phi_0 = -5^o$.

In Fig. 8 the average torque on the shaft becomes three times higher compared to Fig. 6, because the torque signals due to the shifted PM-pairs in Fig. 1 do not overlap. That is to say,

$$\langle T_2 \rangle_{n_c=1} = 3 \cdot \langle T_2 \rangle_0 = 4.52\, mNm. \tag{24}$$

Nevertheless, the form factor of the torque signal is still quite poor. By stacking prime-mover cells in the same shafts as show in Fig. 9, with a suitable angle shift between rotors (multiples of 45^o when $n_c = 8$), a smooth average torque is the outcome (red trace in Fig. 8), with mean value given by

$$\langle T_2 \rangle_{n_c=8} = 8 \cdot \langle T_2 \rangle_{n_c=1} = 36.2\, mNm \tag{25}$$

(see also Table III). It can be shown that above a minimum required value for cell height ($h_c = 12\, mm$ for $2R = 10\, mm$), the vertical separation between stacked rotors barely impacts the torque created by the individual cells.

Aiming at maximizing the utilization of materials, it is opportune to interleave batteries of stacked prime-mover cells

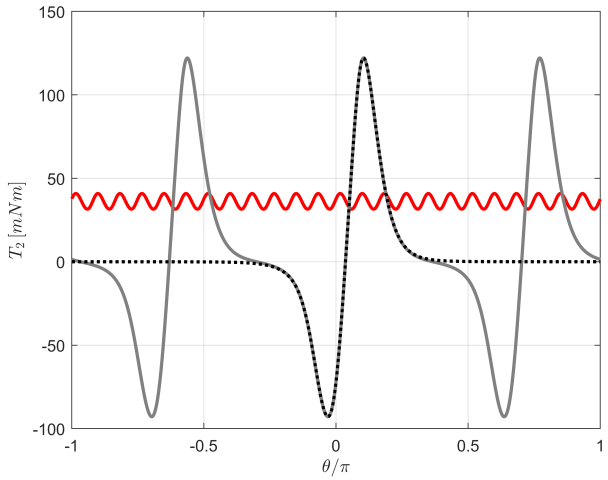

Fig. 8: Static torque profile of a prime-mover cell with 3 PM per rotor ($n_c = 1$, continued trace), and net torque profile (red trace) when stacking multiple prime-mover cells ($n_c = 8$ and $h_c = 12mm$) as sketched in Fig. 9. The dotted trace refers to the torque profile of a simplified cell (see Fig. 6.)

TABLE III: Torque values in Fig. 8

n_c	[-]	1	8	# cells
h_c	[mm]	-	12.0	cell separation
$\langle T_2 \rangle$	[m Nm]	4.52	36.2	net mean torque
T_2^{max}	[m Nm]	122.1	40.9	peak torque

for sharing PMs, as sketched in Fig. 10, resulting a complete magnetic-wind mill. Calculations confirm that the average torque created by the extra force interaction among all PMs located in the 6 cylinders at the periphery of the mill is zero. Consequently, the final average torque on the central axis in

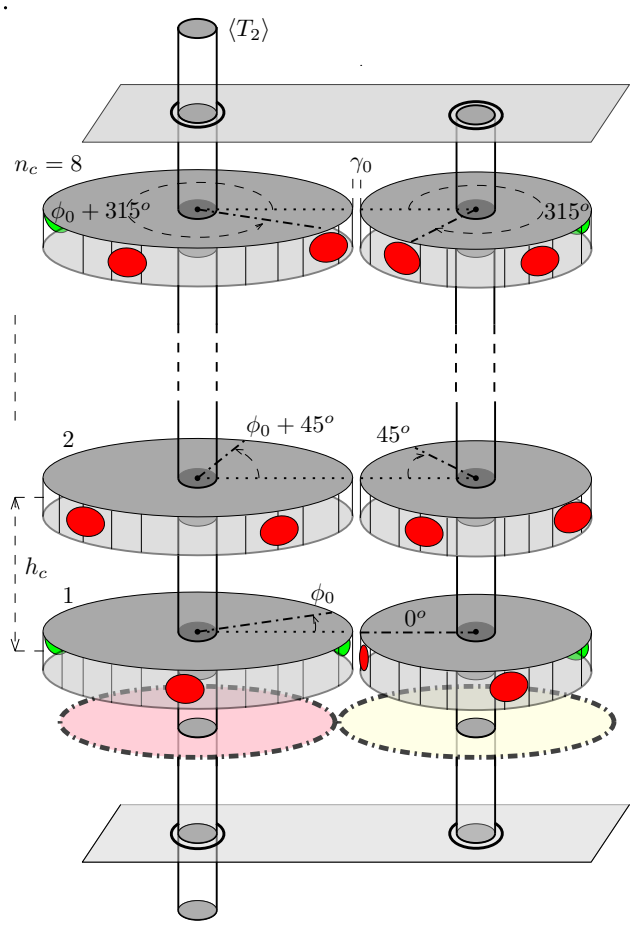

Fig. 9: Layout aiming at engineering a magnetic-wind mill that yields smooth and persistent average torque on the basis of a battery of stacked prime-mover cells.

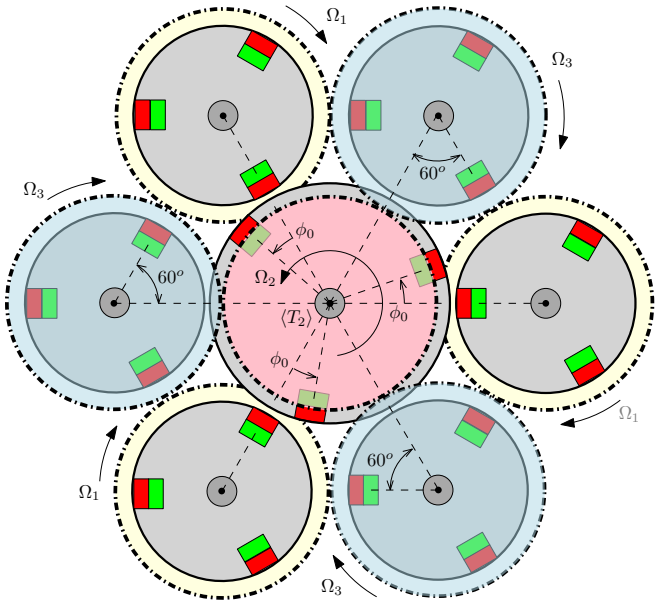

(a) Top view

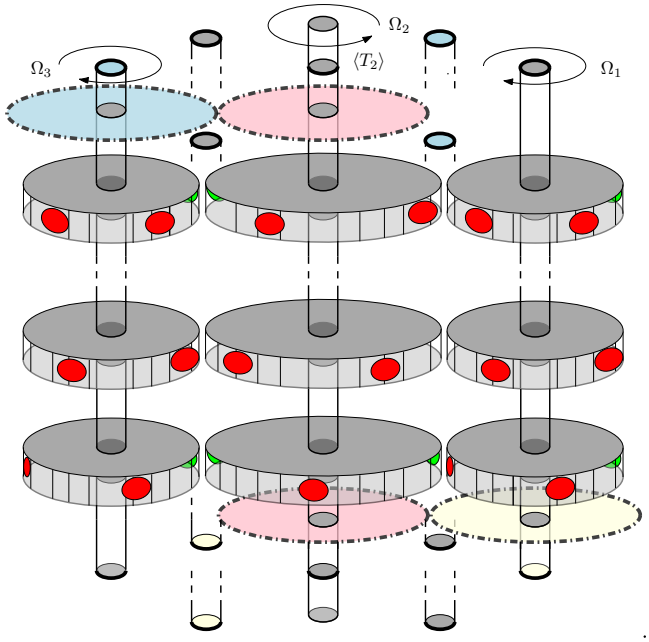

(b) Frontal view

Fig. 10: Layout of a magnetic-wind mill with six interleaved bateries sharing stacked prime-mover cells, for the purpose of maximizing the utilization of the PMs. Note the subtle placement of the cog-wheels.

Fig. 10 is just

$$\langle T_2 \rangle_{n_c=48} = 6 \cdot \langle T_2 \rangle_{n_c=8} = 0.217\, Nm. \tag{26}$$

The resulting torque profile is depicted in Fig. 11.

Altogether, when the central cylinder of the mill is rotating with constant radial velocity Ω_2, the average mechanical power that can be drawn from the spinning axis is found from (26) to become

$$P_2 = \Omega_2 \cdot \langle T_2 \rangle_{n_c=48}\,. \tag{27}$$

For instance,

$$\Omega_2 = 1000\, rpm \;\rightarrow\; P_2 = 22W. \tag{28}$$

It is worthwhile to remark that P_2 in (27) increases proportionally with Ω_2, since $\langle T_2 \rangle$ in (26) is found to be constant, being ideally independent of the rotational speed of the shaft, as justified in the next section.

V. A MAGNETIC-WIND MILL IN THE FIELD

Although the results in Fig. 11 have relation to a static situation, the torque signals may be considered without change in practical dynamic conditions. Since high-quality PM materials have a low relative permeability ($\mu_r \approx 1.03 - 1.05$ for sintered NdFeB) [4], the internal magnetization, $\vec{M}$ as given in (1), is practically not affected by the proximity of another PM with similar characteristics.

Moreover, in view of the extremely low radial speeds in mechanical devices (as the one in Fig. 10) compared to the spreading velocity of EM waves in space, the dynamic regime of the net magnetic field can be considered as quasi-stationary (i.e. virtually instantaneous EM wave propagation).

Hence, from a modeling point-of-view, the currents through

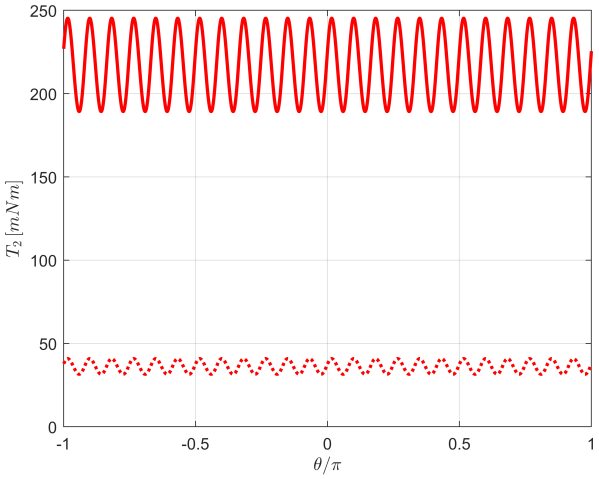

Fig. 11: Net torque characteristics of the mill sketched in Fig. 10, assembled with 6 interleaved batteries sharing prime-mover cells. The dotted trace refers to the net torque of just one battery as in Fig. 9.

the filamentary loops may be assumed to remain constant, independent of the proximity of other loops, even under variable external magnetic flux. The only postulation is that $\mu_r = 1$ in- and outside the PMs.

Bearing in mind the construction of a laboratory prototype for experimental verification, Fig. 12 shows sketches of constituting parts for assembling a magnetic wind mill to operate in the field. It is expected that the maximum power that can be unfolded with the device will be limited by the vibrational stability of the mechanical part and by the induced eddy currents in the PM materials.

The PM magnetization, as such, is not directly impacted by electromotive forces (EMF) as induced by a time-changing magnetic flux due to the translation of neighbor PMs in the surrounding space. Nevertheless, by its turn this induced emf will produce eddy currents, therefore losses, in the PM material.

Magnet losses are usually neglected for plastic bonded or ferrite PMs, due to their quite high material resistivity. However, the resistivity of rare-earth magnetic materials (like NdFeB) is much lower, and eddy-current losses may increase the PM temperature to a point that the remanent magnetic flux density is noticeably affected, decreasing the PM performance as a consequence, as it is the case in high-speed PM motors [5].

VI. Discussion

Imagine the two current loops in Fig. 3 are realized with copper wires (as in an electromagnet), these windings being fed from electrochemical batteries in combination with electronic circuits. Feedback control is then applied for the purpose of keeping constant the currents through the circular windings during the spatial translation of the moving loops. The outcome of (22) forecasts that the two moving windings

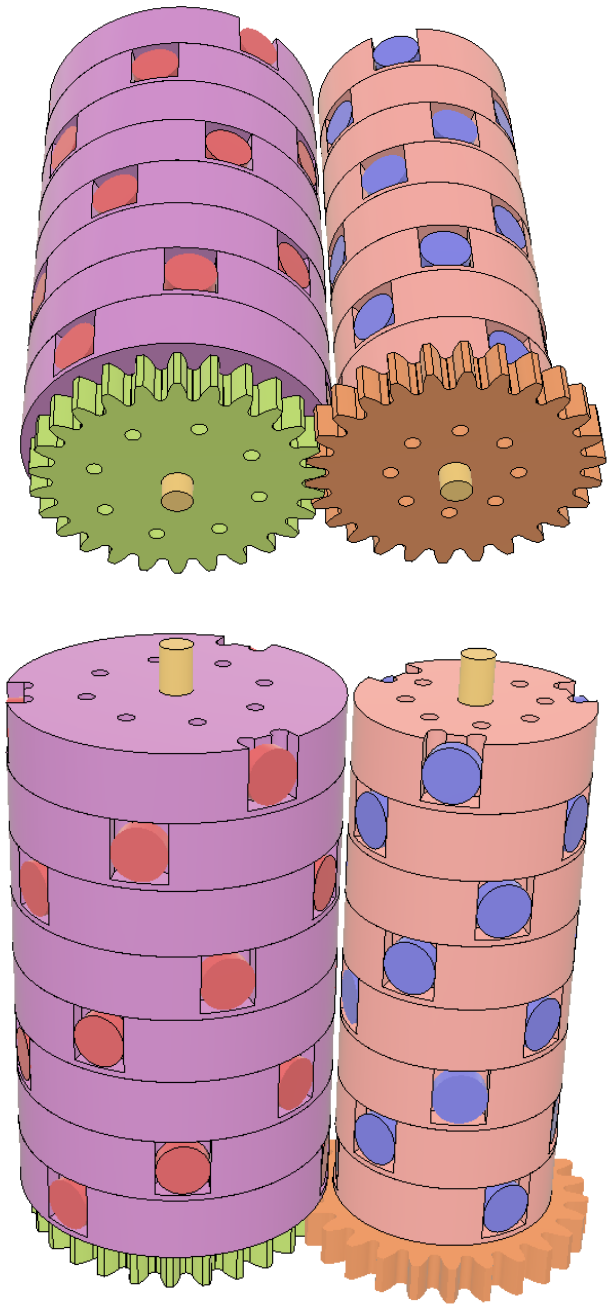

Fig. 12: Impression of mechanical parts for a mill prototype

will be accelerated up to the radial velocity for which equilibrium is reached between the introduced energy excess per turn and the power dissipated in the wires (due to current circulation) plus the power dissipated by friction in the moving parts of the system. Thereby, an engineer would not doubt that manufacturing this sort of exotic electric motor is feasible, since the dimensioning of it can be done on the basis of well-established formulas from the Classical EM Theory, with the conviction that the power dissipated by friction and heat is delivered by the **batteries** that drive the windings!

Already from the beginning of the 19th century, a well-accepted model for describing the behavior of PMs can be obtained by means of **constant** electric currents circulating

on the external surface of the magnetic material, the so-called Amperian currents in (3). These imaginary superficial currents are the macroscopic equivalent representation of the microscopic atomic activity of the internal particles of the material. In this way, the magnetic field as created by (a superposition of) filamentary current loops with constant current is generally accredited as a simple, yet quite effective, model of a PM. In this representation, the formulas for calculating forces between PMs are exactly the same as the ones used for calculating the forces between electromagnets.

Therefore, it is remarkable that the prognostic of (22), based only on purely analytical equations that have been applied and exhaustively verified by experiments for more than a century, asserts that a privileged translation of PMs (modeled as a superposition of linear loops with constant current) will deploy **sustainable energy** from the sources that keep the Amperian currents constant during the trajectory.

So, the outcomes of seminal equations is that the source of energy that keeps going on the microscopic atomic activity in a PM, is the same source that delivers the excess energy at every revolution of the current loops, without recurrence to any further assumption.

In Sec. 4 of [1] an interpretation is given for the energy source that propels the microscopic activity of the internal particles in a PM, resorting to elementary notions from Quantum Electrodynamics. Nevertheless, aiming at an engineering project the supposition of constant Amperian currents is enough for designing and assembling prototypes.

VII. Conclusion

The design methodology in this article starts from the portrayal of elementary prime-mover cells with PMs only. Subsequently, these cells are stacked to form batteries, and after that, batteries are interleaved to construct a mill in such a way that significant and persistent torque develops on the shaft to perform useful work. Even though the discussion only introduces concepts from classical Electromagnetism, supposedly considered a ”completed” theory in so many books on Physics, the next mandatory step to clarify the defiant theoretical outcomes will be, of course, to assemble a prototype with enough dexterity for conclusive experimental verification.

Acknowledgements

We would like to thank L. Kurmann, J.J. Brilman and M.A.M. Hendrix for the valuable discussions.

References

[1] J.L. Duarte. *Modeling the Yildiz Motor revisited*. Eindhoven University of Technology Research Report. July 2018. https://doi.org/10.6100/6b67487a-bd78-4a24-bdd1-d7b9b3dbd5b7

[2] L. Kurmann and J.L. Duarte. *Generation of asymmetric incommensurable torque signals*. Journal of Physics: Conference Series, [PW-17f]. POWERMEMS Int. Conf., Dec. 2018.

[3] S. Babic and C. Akyel. *Magnetic Force Between Inclined Circular Filaments Placed in Any Desired Position*. IEEE Trans. Magn., vol. 48, no. 1, pp. 69-80, 2012.

[4] E.P. Furlani. *Permanent magnet and Electromechanical Devices: materials, analysis and applications*. Academic Press, London, 6th ed., 2001.

[5] J.L.F. van der Veen, L.J.J. Offringa and A.J.A. Vandenput. *Minimising rotor losses in high-speed high-power permanent magnet synchronous generators with rectifier load*. IEE Proc., Electr.Power Appl., vol. 144, pp. 331-337, 1997.

Eindhoven, February 11th, 2019
J. L. Duarte